

Particle rotation of granular materials in plane strain

Zhibo Chen PhD, A.M.ASCE

PhD Candidate, Civil & Urban Engineering Department, NYU, Brooklyn, NY, USA

Mehdi Omidvar PhD, A.M.ASCE

Assistant Professor, Civil and Environmental Engineering Department, Manhattan College, Riverdale, NY, USA

Kaigang Li MS

R&D Analyst, AIG Science, New York, NY, USA

Magued Iskander PhD, PE, F.ASCE

Professor and Chair, Civil & Urban Engineering Department, NYU, Brooklyn, NY, USA (corresponding author: Iskander@NYU.edu)

Important aspects of collective behaviour in granular media, such as formation of force chains and shear localisation, are related to kinematics at the underlying particle scale. Particle kinematics consists of translation and rotation. While considerable effort has been dedicated to resolving the translational component of particle displacements, rotational components have received less attention that is due partly to the difficulty associated with distinguishing rotation from translation at the particle scale. In this paper, three new methods based on digital image correlation, image registration and point least-square estimation are introduced to quantify planar particle rotation. The underlying theory behind each method is described and the performance of the methods is assessed through detailed error analysis. The strengths and weaknesses of each method are discussed based on their applicability to study particle kinematics in natural sand. The methods are presented in the form of open-source codes that can be integrated with other analytical tools to investigate particle kinematics. The application of the three methods is demonstrated through the study of particle rotation in plane strain assemblies of granular media under active and passive conditions.

Notation

C covariance matrix

c scale factor

U, V orthogonal matrices

D diagonal matrix

n number of points

R, T rotation and translation components

X, Y displaced and original location of the particle

$\mu_p, \mu_{p'}$ mean vectors of P_i and P'_i

Image-based experimental techniques have been shown as a valuable tool for investigating particle kinematics in granular materials (Hall *et al.*, 2010; Omidvar *et al.*, 2014; Paikowsky and Xi, 2000; von Pokorný and Horender, 2014); however, there are still several remaining challenges. First, the success rate in uniquely identifying and segmenting individual irregular-shaped particles decreases significantly if the studied granular material is densely packed and/or susceptible to grain crushing (Andò *et al.*, 2012). Second, although particle rotations have been observed during the flow of granular materials, especially around shear bands (Oda and Konishi, 1974; Roscoe and Schofield, 1964), most particle tracking algorithms focus solely on capturing the trajectories of particle centroids, neglecting particle rotation. Nevertheless, particle rotation has been recognised as an important mechanism affecting the behaviour of granular soils, especially when inter-particle friction is large (e.g. Bardet and Proubet, 1992; Oda and Kazama, 1998; Oda *et al.*, 1982).

In this paper, three newly developed methods that are able to capture the two-dimensional (2D) rotations of granular assemblies are introduced. The accuracy of each method is assessed, and its advantages and disadvantages are discussed. In addition, the applicability of the three methods to study

1. Introduction

Granular materials are conventionally studied as continua where global measurements of stress and strain are collected for analysis in spite of granular materials consisting of individual particles and voids. The limitations of such approaches were recognised in the early twentieth century (Terzaghi, 1920). Numerous studies in soil mechanics have revealed that observed macroscopic behaviours of granular materials are in fact greatly influenced by mechanisms occurring at the particle level (Baudet *et al.*, 2010; Hall *et al.*, 2010; Matsuoka, 1974). Phenomena, such as the formation and buckling of force chains, dilation and shear localisation, are more appropriately elucidated at the particle scale (Omidvar *et al.*, 2012).

granular material is demonstrated through preliminary experiments conducted on assemblies of dual-sized plastic circular rods placed in a plane strain chamber. The chamber is subjected to wall rotation about its toe to simulate active and passive conditions, and particle rotations are demonstrated. The algorithms are developed in Matlab and are made available as an open-source code.

2. Experimental set-up

2.1 Test materials

The granular material used in the experiments is comprised of high-density polyethylene rods (HDPE) manufactured by US Plastic Corp (USP). The density, compressive modulus and coefficient of friction are reported by the manufacturer as 969 kg/m^3 , 689.5 MPa and 0.28 (16°), respectively. HDPE was chosen due to its rigidity, light weight and easy machining properties. The 50 mm (2") long cylindrical rods are cut and machined from 2.4 m (8') long stock having two diameters of 25.4 and 12.5 mm (1" and 0.5"). The surface of the rods is milky white with little texture. The algorithms developed to track the rotation of each particle require some texture or certain surface features. Hence, one side of the flat faces of the rods are patterned with speckle using spray paint; the other side of the flat faces of the rods are marked with two 3.2 mm (1/8") dia. red and green adhesives (Figure 1). After face treatment, the 50 mm (2") long rods are mixed thoroughly in a container using a mixing ratio of 50:50 (by number). The mixed rods are then randomly dropped into the test chamber so that

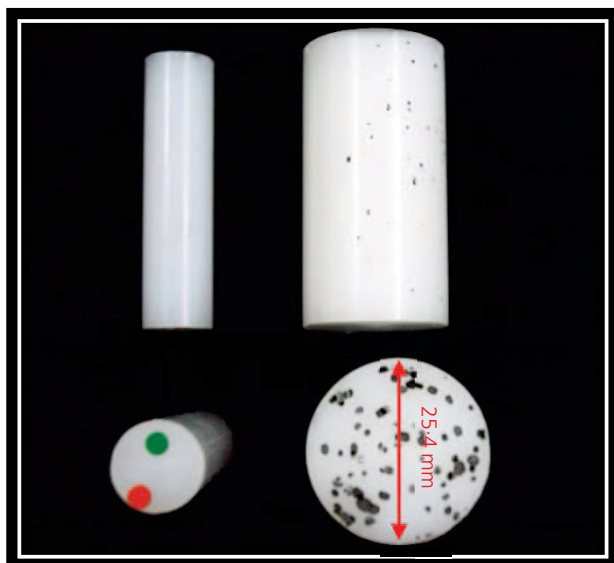


Figure 1. Image of face treated HDPE

the spray painted side is on one side of the chamber while the dotted side is on the other.

2.2 Test chamber

The experiments are performed in an acrylic plane strain chamber with the dimensions shown in Figure 2. The use of acrylic panels allows observation of particle kinematics from both the front and rear sides of the chamber. The acrylic observation windows are separated on the sides by an aluminium wall. The thickness of the aluminium precisely matches the thickness of the HDPE rods, with a tolerance of 0.1 mm (4×10^{-3} inches). A thin adhesive, $\sim 0.1 \text{ mm}$ thick, is placed between the interface of the aluminium wall and the polycarbonate panels to allow the free fall of mixed rods into the chamber, and to reduce friction between the granular assemblies and the acrylic panels. The aluminium wall inside the chamber is hinged at the base of the chamber to allow wall rotation about its toe. A micrometre is installed at the top of the wall to permit precise incremental movement against or away from the granular assembly so as to simulate passive and active conditions.

2.3 Image acquisitions system

During the experiments, digital images are acquired after every increment of wall movement by two Nikon D3200 cameras (front and back). The cameras are positioned at a distance of $53.5''$ (1359 mm) from the chamber front and rear panels so that the image plane of each camera is parallel to the chamber walls. The cameras are synchronised using a programmable remote trigger. Both cameras have a resolution of 24 Mpx (6000×4000) and are equipped with an $18\text{--}55 \text{ mm}$ Nikon zoom lens set to f/5. The acquired images have a spatial resolution of 180 px per inch (25.4 mm). Consequently, small and large diameter particles have a spatial resolution of $\sim 90 \times 90$ and $180 \times 180 \text{ px}$, respectively.

Ambient lighting is found to produce adequate uniform illumination for imaging both sides of the chamber. The acquired images are stored in raw image format to avoid compression prior to conversion to RGB colour images and subsequent 8-bit grey-scale TIFF conversion for image processing purposes. Image scale is converted to physical units by employing a standard calibration chart.

2.4 Test procedure

A series of four tests are conducted (Table 1). The tests are classified based on their wall surface condition and wall movement. In the two active tests, the wall rotates away from the granular assemblies at an increment of $\Delta/H = 0.005$ (0.287°), where Δ is the horizontal displacement of the micrometre and H is the initial height of the sample. In the two passive tests, the wall rotates against the granular assemblies at an increment

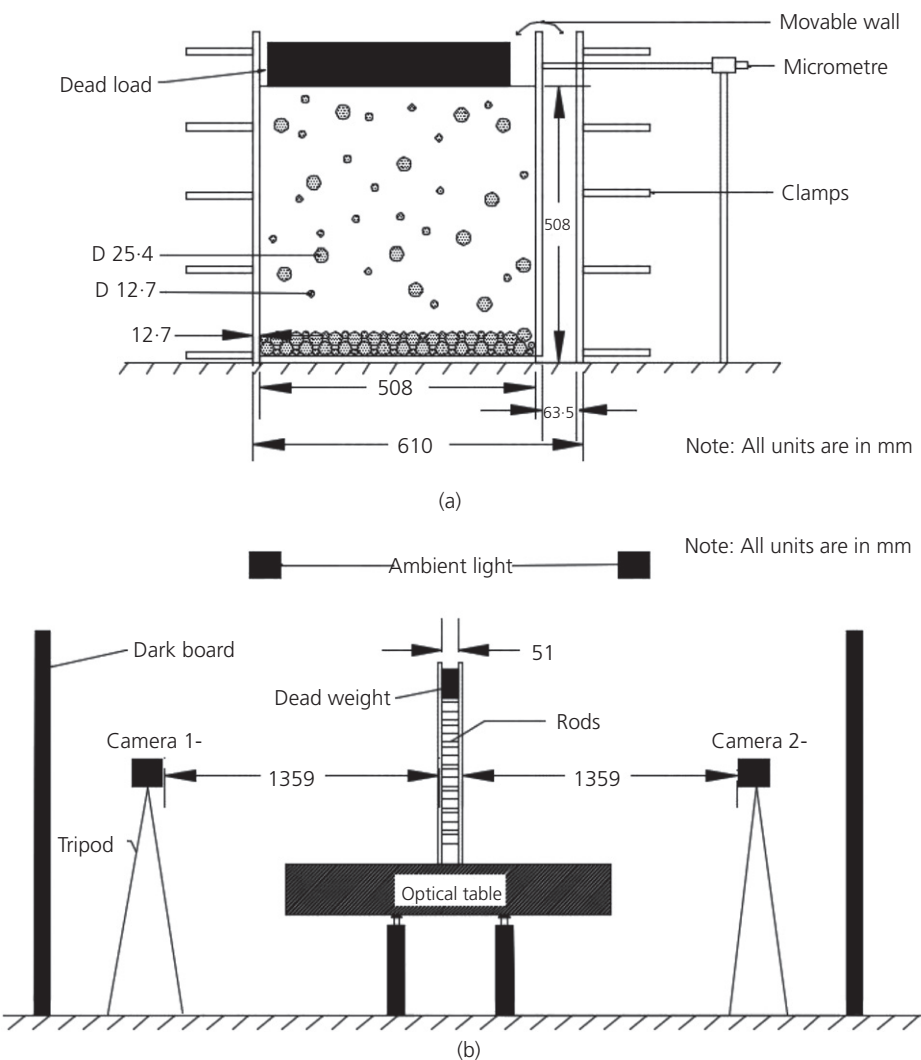


Figure 2. Schematic drawing of the experimental set-up: (a) front view and (b) side view

Test number	Wall surface condition	Wall movement
1	Smooth	Active
2	Smooth	Passive
3	Rough	Active
4	Rough	Passive

Table 1. Test list

of $\Delta/H = 0.005$ (0.287°). Among the four tests, two are conducted with the wall surface roughened by gluing sand paper of grade 40 to the wall. For all four tests, a small surcharge of

8.3 kPa is applied at the surface of the granular assemblies using steel bars as dead weights.

3. Particle identification and tracking

Image analysis is performed on acquired images to resolve particle kinematics. The key analyses include image preprocessing, particle identification, particle tracking (centroids only) and particle rotation. This section outlines the main processes associated with particle identification and tracking.

3.1 Image preprocessing

Various image preprocessing techniques can be used to enhance the image quality so that more particles can be identified accurately. The main goals of image preprocessing are to

enhance contrast and remove non-uniform illumination. In this study, the following three preprocessing steps are performed on each image using open-source software ImageJ (Rasband, 1997–2016): (a) image inversion, (b) sliding paraboloid background subtraction and (c) image normalisation. Examples of preprocessed and postprocessed images are shown in Figure 3. Details of the three preprocessing algorithms can be found in Rasband (1997–2016).

3.2 Particle identification

The granular material employed in this study is densely packed; these are circular in cross-section. A popular approach for identifying circular objects in images is through circular Hough transform (CHT). There are many different implementations of CHT (e.g. Atherton and Kerbyson, 1999; Peng

et al., 2007; Yuen *et al.*, 1990). Atherton and Kerbyson's phase coding method, implemented in the Matlab function 'imfindcircles', is used to identify the particle centroids and radii. The function requires input of radius range, object polarity, computation method, sensitivity factor and edge threshold. Object polarity quantifies the extent to which circular objects are brighter or darker than the background. Sensitivity factor is the sensitivity to the CHT accumulator array. Edge threshold sets the gradient threshold for determining edge pixels in the image. A sensitivity factor that is >0.95 and an edge gradient threshold <0.05 is employed. These parameters are selected by trial and error to increase the percentage of accurately identified particles. However, this choice of parameters increases the risk of false positives stemming from weak edges and obscured circles. Nevertheless, most false particles identified in each image are eliminated through the particle tracking process

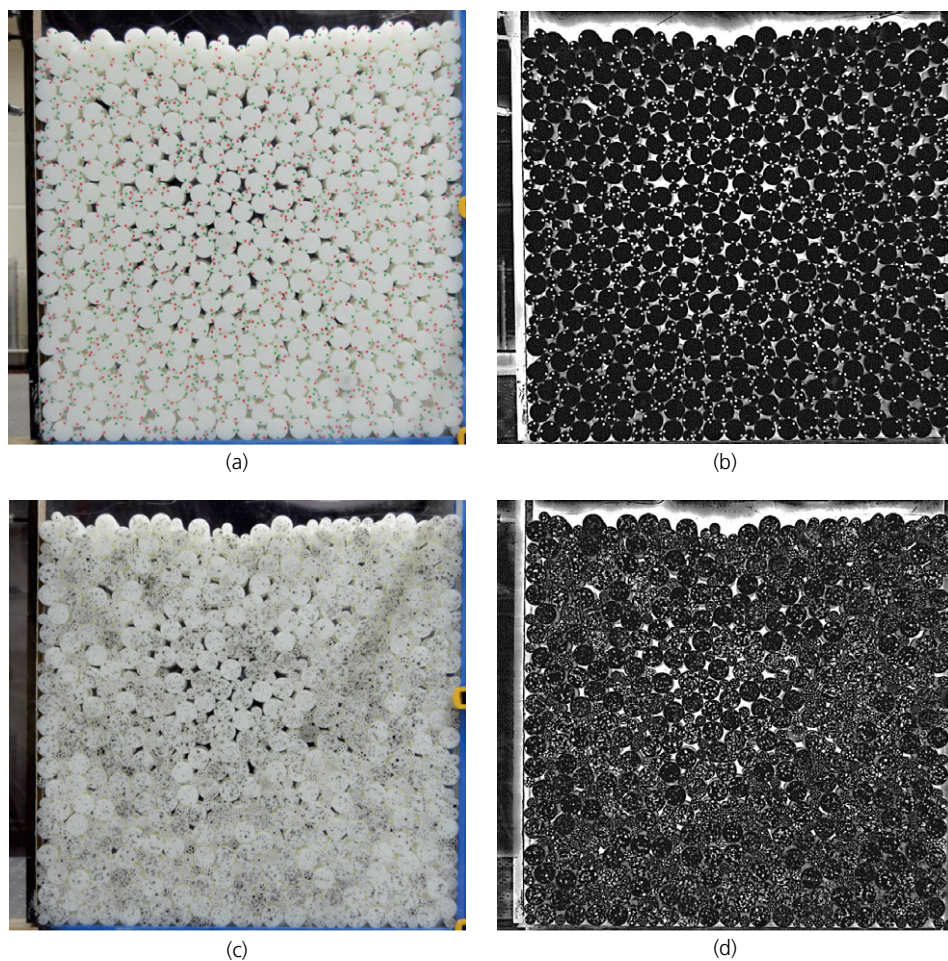


Figure 3. Test images: (a) original dotted HDPE image, (b) preprocessed dotted HDPE image, (c) original speckled HDPE image and (d) preprocessed speckled HDPE image

where only particles with full trajectories are retained. The speckle pattern added to each particle for particle rotation calculation has a negative impact on the accuracy of particle identification. Accordingly, speckled particles of two different diameters are identified separately and then the two separate identification results are combined together; however, the accuracy of identifying speckled particles is still lower than that of dotted particles (Figure 4).

There are two types of errors associated with particle identification. The first type of error is false identification or particle omission. Based on typical particle identification results, an example of which is shown in Figure 4, the dotted particle image has an identification success rate of 99%, while the speckled particle image has an identification success rate of 91%. Thus, 99 and 91% of the particles are correctly identified in the dotted and speckle particle images, respectively. The success rates are obtained by manually comparing the total number of particles in the image with the number of particles that are falsely identified or omitted. The second type of error is associated with accurately identifying the location of the centroid of each particle. This type of error is reported to be inversely proportional to the particle image diameter (D), in pixels, for spherical particles (Hunter *et al.*, 2011). Omidvar *et al.* (2014) has also reported an error of $\sim 0.03D$ for silica gels that are less circular than the rods used in this study.

The approach described for particle identification can be used only for circular objects. The identification of densely packed irregular-shaped particles remains an active research problem. The main challenges are to: (a) distinguish the crowded particles from the background and (b) segment adjoining particles

into their correct shape. Advanced imaging techniques, such as adaptive thresholding (Carpenter *et al.*, 2006) and morphologic reconstruction (Zheng and Hryciw, 2016), have been developed to tackle these challenges; the success rate, however, remains somewhat limited. One way to get around the problem is to employ multiple colour dyes to stain the test sand prior to imaging. In this way, the coloured soil particles can be identified through binarisation. This physical separation approach does not allow for the identification of all soil particles in an image, but a significant amount of irregular-shaped soil particles can be identified this way.

It is important to point out that circular objects are only required for particle identification. The developed algorithms for particle tracking and rotation calculations do not have such constraints and these can be used for irregular-shaped particles if the particles can be identified correctly prior to particle tracking.

3.3 Particle tracking

After particle identification, the centroids and radii of particles in each image are saved in matrix format. Particle trajectories can then be obtained by tracking the positions of particle centroids in consecutive images. The trajectories include only the translational movement of the particles, not their rotation.

In this study, the tracking algorithm developed by Crocker and Grier (1996) is employed to track particle translation. The algorithm assigns a user defined search radius to particle centroids in the original image, and searches for their corresponding new locations in subsequent images. An optimisation

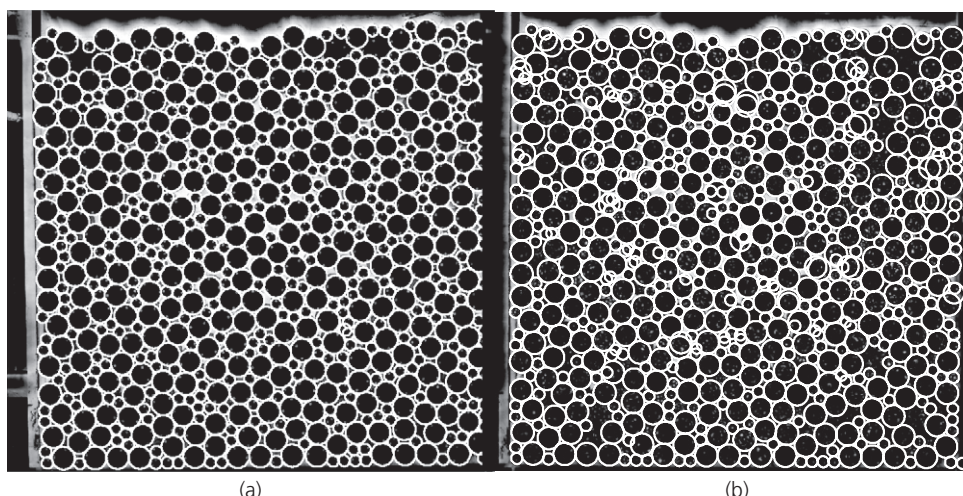


Figure 4. Images of particle identification: (a) dotted HDPE image and (b) speckled HDPE image

algorithm is performed, whereby the minimum squared difference of the neighbouring centroid positions in the search radius is used to identify particle translations (Figure 5). The recommended search radius is a value limited to the mean spacing between the particles. As a result, successful identification of particle kinematics between global rotation increments of the wall requires that inter-frame particle translation be limited to the radius of the 0.5" (12.5 mm) dia. rods. Particle translations exceeding the above-mentioned threshold are not captured by the algorithm, and the corresponding particle is excluded from further analyses. This process is repeated so that the locations of the centroid of each particle of an image sequence are uniquely identified. Only particles with fully resolved trajectories are considered for further analysis; particles that do not have full trajectories are eliminated.

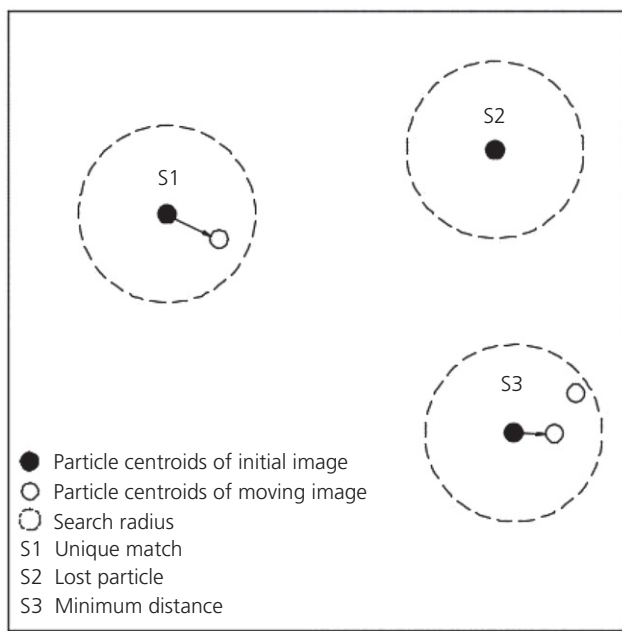


Figure 5. Particle tracking processes

4. Particle rotation algorithms

Three different approaches have been developed for calculating particle rotation from a series of acquired images. Methods 1 and 2 are used with speckled particles, while Method 3 is employed with pre-marked dotted particles. Each approach offers certain advantages depending on the images being analysed, as discussed in the respective sections.

4.1 Method 1: particle-level digital image correlation (DIC)

The first method developed to calculate particle rotation of 2D granular assemblies combines the results of particle tracking and DIC. DIC is a well-established pattern recognition technique for measuring deformations by comparing grey-scale images before and after deformation. The DIC algorithm subdivides images into smaller interrogation windows, and performs an optimisation analysis between corresponding windows to determine its displacement magnitude and direction. The main processes involved in a typical DIC analysis are schematically presented in Figure 6. The fundamental premise of Method 1 is that movements of individual particles can be resolved using DIC analysis within the particle boundaries if sufficient resolution and texture is present within the acquired particle image. This is somewhat different than conventional DIC analysis where the interrogation window typically contains a few particles, and the obtained displacement vector represents the average movement of the particles within the interrogation window. Conventional DIC is a powerful tool to investigate meso-scale deformations of granular materials (e.g. Hall *et al.*, 2010; Omidvar *et al.*, 2014; Rechenmacher *et al.*, 2010). In this study, the DIC approach is adapted to obtain micro-scale rotational components of particle kinematics. A particle is, therefore, subdivided into multiple interrogation windows and the corresponding displacement field can be used to extract particle kinematics, including translation and rotation. A somewhat similar approach has been employed by Andò *et al.* (2012) to resolve particle scale kinetics by using X-ray tomography.

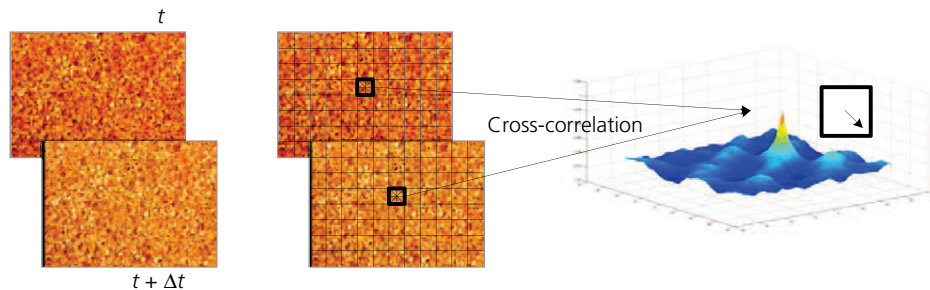


Figure 6. The main processes of DIC analysis

Particle tracking yields matrices that assign a unique identification number to each particle along with the coordinates of the centroid location of every particle and their associated radii for a sequence of images. A search algorithm then identifies the DIC vectors contained within each particle, and associates these vectors with the given particle. The displacement vectors within each particle are then separated into a translation and a rotation component. This is done by assuming the translation component to be equal to the predicted translation from the particle tracking analysis for each particle. The rotational component is then the difference between the DIC displacement vectors within the particle and the translation from the particle tracking analysis. The magnitude and direction of particle rotation can be calculated using the centroid of the particle and the displacement magnitudes.

The algorithm, schematically illustrated in Figure 7, can be described as follows.

- (a) Perform DIC analysis for a sequence of images, ensuring that each particle contains multiple interrogation windows (preferably more than three across).
- (b) Based on the previously obtained particle tracking results for each image pair
 - (i) extract DIC displacement vectors contained within each particle (Figure 7(a)) and assign it to the given particle
 - (ii) find the particle centroid translation (Figure 7(b)).
- (c) Subtract centroid translation from the extracted DIC displacement vectors contained within the particle to isolate particle rotational components (Figure 7(c)).

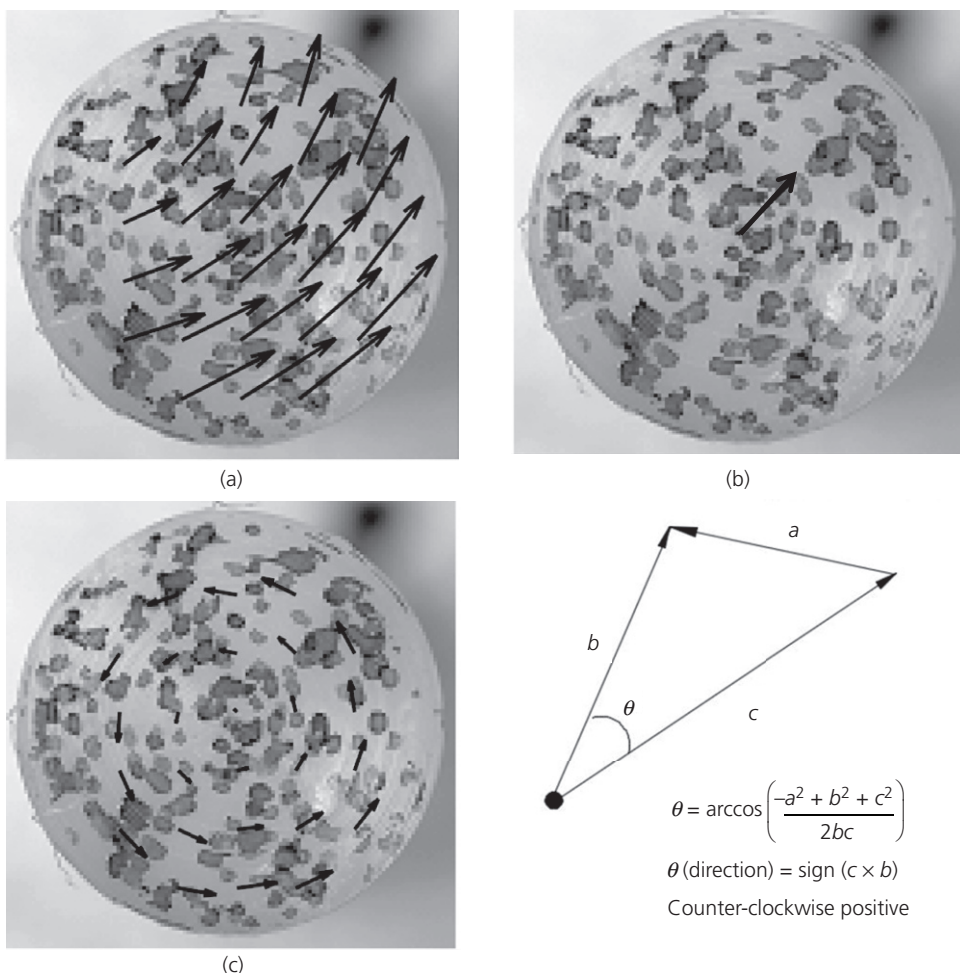


Figure 7. The main steps of Method 1 to obtain particle rotation:
(a) DIC displacement vectors, (b) particle centroid translation,
(c) particle rotational components, (d) cosine rule and vector
calculus

- (d) Calculate the angles of rotation based on the rotational vectors within the particle, using trigonometry (Figure 7(d), cosine rule).
- (e) Calculate the median value of the calculated rotation angles within the particle as its rotation angle.
- (f) Determine the direction of rotation using the cross-product of the two vectors connecting the particle centroid and the initial and end points of the rotational vector within the particle (counter-clockwise is positive).
- (g) Repeat steps (b–f) for every particle.

4.2 Method 2: intensity-based image registration

The particle identification and trajectory information can be used to isolate particles for image registration to calculate rotation. The displaced location of a particle can be described as an affine transform

$$1. \quad Y = RX + T$$

where X and Y are the displaced and original locations of the particle, R and T are the rotation and translation components. In this method, for each particle, a square mask is first applied over the image so that only the particle is retained, nulling the remainder of the image (Figure 8). This process removes the translation component, T . The rotation component is then a 2D matrix

$$2. \quad R = \begin{pmatrix} \cos \theta & -\sin \theta \\ \sin \theta & \cos \theta \end{pmatrix}$$

The algorithm for calculating particle rotation can be described as follows.

- (a) For each particle in a displacement increment image pair, construct a square binary mask centred at the particle centroid, both in the original and deformed images. Choose the width of the square mask so that it is equal

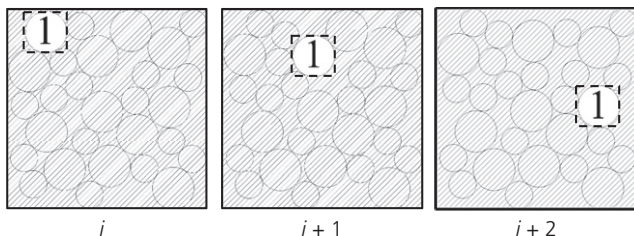


Figure 8. Removing translation component of a particle based on particle tracking results

to the diameter of the identified particle. The result is a set of two independent images of the particle in the original and deformed images. Once the images are independently cropped, any translation information is lost and the only difference between the two images is the particle rotation (Figure 9).

- (b) Correlate the two particles using the Matlab built-in function ‘imregtform’. This function estimates the geometric transformation between an image pair by means of ‘regular step gradient descent optimisation’ with a mean square error metric. More information about the function is found in Mathworks (2013).
- (c) Store the result of the correlation in a 2D matrix, R . This is essentially an affine transformation characterised solely by rotation, since translational information is lost due to application of the mask.
- (d) Use the obtained rotation matrix R to calculate the particle rotation angle between the image pair.
- (e) Repeat steps (a–d) for all particles, in all image pairs.
- (f) The magnitude and direction of the rotation angle of the particle can be calculated as

$$3. \quad \theta = a \tan 2d(\mathbf{R}(2, 1), \mathbf{R}(1, 1)) = a \tan 2d(\sin \theta, \cos \theta)$$

4.3 Method 3: least-square points estimation

Similar to Method 2, in Method 3 unique patterns on particle are used to define an affine transformation, from which the rotation component can be extracted. In this method, the dotted particle images are used. First, a mask similar to Method 2 is applied on each particle. To calculate the particle rotation, Method 3 finds the transformation parameters between two point patterns through least-squares estimation (Umeyama, 1991)

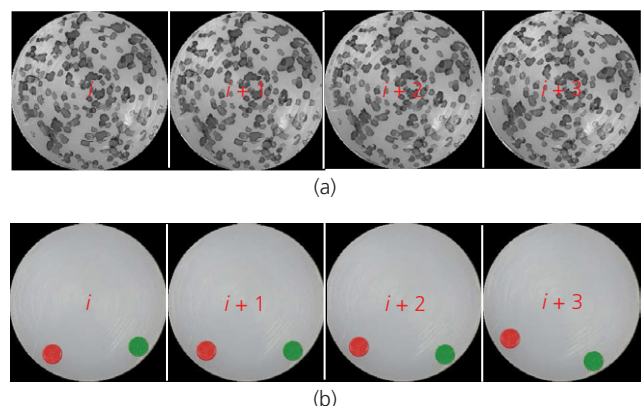


Figure 9. Cropped image sequence of an individual particle: (a) speckled face and (b) dotted face

Given two sets of corresponding points $P_i = \{x_1, x_2, x_3, \dots, x_n\}$ and $P'_i = \{x'_1, x'_2, x'_3, \dots, x'_n\}$ in 2D space, there exists a transformation

$$4. \quad P'_i = c\mathbf{R}P_i + \mathbf{T}$$

where c is a scale factor between the two reference images. In this study, for any cropped image pair, c and \mathbf{T} are approximately equal to one and zero, respectively. Hence, the transformation Equation 5 can be simplified as

$$5. \quad P'_i = \mathbf{R}P_i$$

For a set of n points, \mathbf{R} can be obtained through least-squares estimation. First, the covariance matrix \mathbf{C} of P_i and P'_i is obtained

$$6. \quad \boldsymbol{\mu}_p = \frac{1}{n} \sum_{i=1}^n P_i$$

$$7. \quad \boldsymbol{\mu}_{p'} = \frac{1}{n} \sum_{i=1}^n P'_i$$

$$8. \quad \mathbf{C} = \frac{1}{n} \sum_{i=1}^n (P'_i - \boldsymbol{\mu}_{p'}) (P_i - \boldsymbol{\mu}_p)^T$$

where $\boldsymbol{\mu}_p$ and $\boldsymbol{\mu}_{p'}$ are mean vectors of P_i and P'_i , and n is the number of points. Then, a singular value decomposition is performed on \mathbf{C} such that

$$9. \quad \mathbf{C} = \mathbf{UDV}^T$$

where \mathbf{D} is the diagonal matrix containing singular values of \mathbf{C} , and \mathbf{U} and \mathbf{V} are the orthogonal matrices. When rank $(\mathbf{C}) \geq m - 1$, \mathbf{R} can be determined uniquely as follows

$$10. \quad \mathbf{R} = \mathbf{USV}^T$$

where \mathbf{S} must be chosen as

$$11. \quad \mathbf{S} = \begin{cases} I & \text{if } \det(\mathbf{U}) \det(\mathbf{V}) = 1 \\ \text{diag}(1, 1, \dots, 1, -1) & \text{if } \det(\mathbf{U}) \det(\mathbf{V}) = -1 \end{cases}$$

After obtaining \mathbf{R} , the magnitude and direction of the rotation angle of the particle can be calculated using Equation 3.

In order to generate two sets of corresponding points P_i and P'_i for a pair of cropped particle images, two colour adhesives were attached onto the surface of each particle, opposite to the speckled surface. By doing so, three unique points can be identified and extracted for each cropped particle image; these are the centroids of the particle, the red adhesive and the green adhesive. The x and y coordinates of the three unique points of the initial image and the moving image are the corresponding points P_i and P'_i . The coordinates of the particle centroids are obtained through particle identification. The coordinates of the centroids of the red adhesives are obtained through two steps. First, for each cropped particle image, extract the red component of the image only and then binarise it. This means the binarised image would become black everywhere except where the red adhesive is. Second, use Matlab built-in function ‘regionprops’ on the binarised image to extract the coordinates of the centroid of the red adhesive. More information about the function is found in Mathworks (2006). The coordinates of the centroids of the green adhesives can be obtained similarly by extracting the green component of each cropped particle image. The centre of rotation is the particle centroid since the coordinates of the particle centroid stay constant between any cropped image pair.

5. Performance of proposed methods

5.1 Errors in the proposed methods

Sources of error for the methods developed could emerge in three calculation steps: (a) particle identification, (b) particle tracking and (c) particle rotation. Errors associated with particle identification and tracking are rather small for good image sequences, although these may vary greatly depending on image quality and magnitude of particle motion between frames. Thus, the main focus of this section is to quantify the errors associated with the developed methods in calculating particle rotation.

To quantify the errors of each method, images of a particle having different resolutions are digitally rotated by 0·1–20° and compared with the predicted rotation from the three methods. These values are chosen to represent possible range of particle rotations between any two consecutive images. In most experiments, users are expected to minimise error by controlling anticipated particle rotations between consecutive images. However, for applications where a large deformation is expected to occur in a short period of time, large particle rotations cannot be avoided, and Method 1 should not be used. The observed errors are presented in Figure 10 as a percentage of the applied rotation. A number of important observations can be made. First, the error in calculating

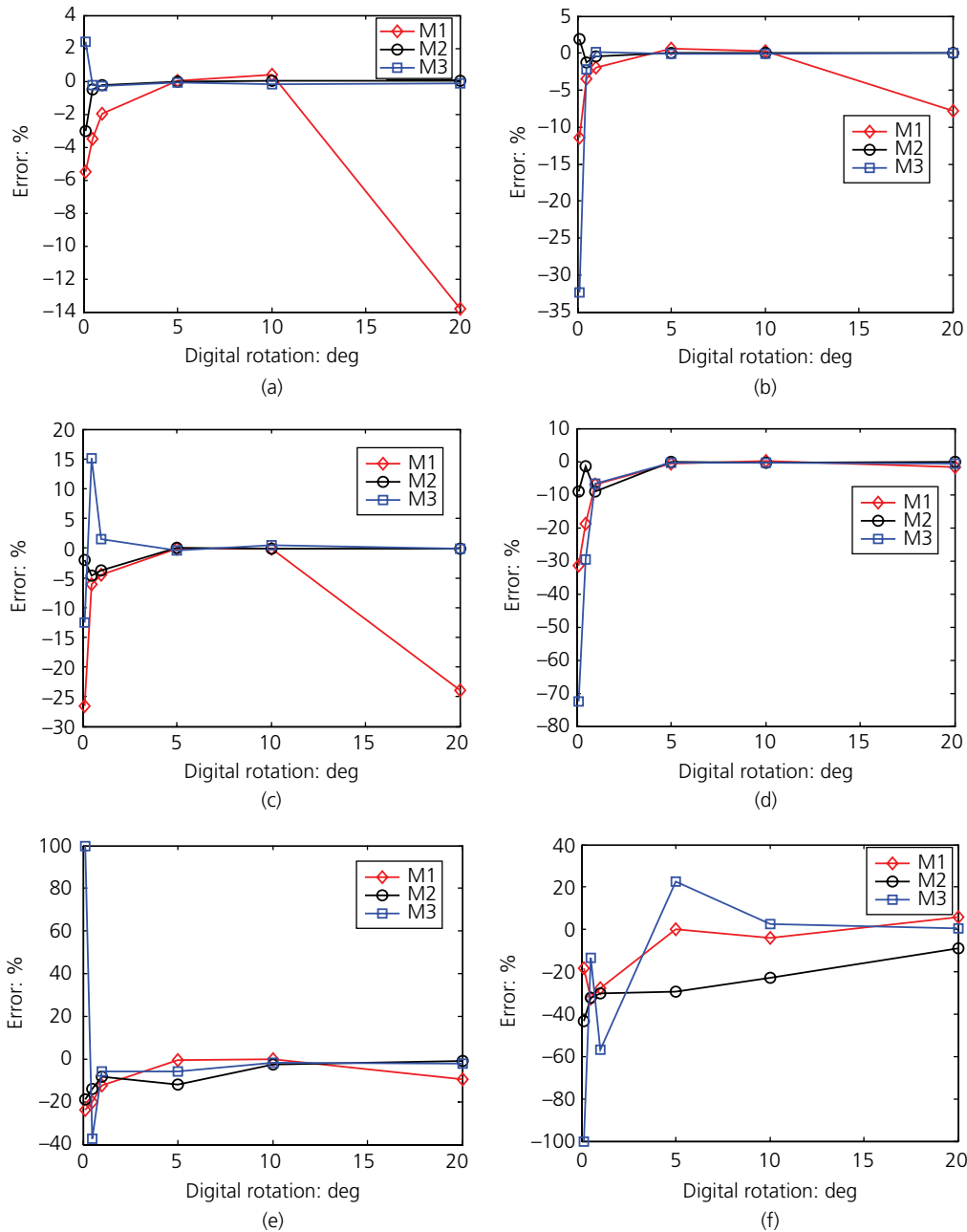


Figure 10. Percentage error of the calculated particle rotation of various particle diameter resolution (PDR) for three different methods against a set of digital rotation ($0\text{--}1^\circ$, $0\text{--}5^\circ$, 1° , 5° , 10° , 20°): (a) PDR = 960 px, (b) PDR = 480 px, (c) PDR = 240 px, (d) PDR = 120 px, (e) PDR = 60 px and (f) PDR = 30 px (positive indicates over-estimation and vice versa)

particle rotation for all three methods increases with decreasing particle resolution. Second, large errors can be expected for rotation of $<1^\circ$, especially for low-resolution particles. Third, the majority of errors are negative, indicating that the calculated rotation angle tends to be smaller than the actual rotation. Fourth, a majority of errors rapidly converges to zero

as the angle of rotation increases beyond 1° , with some exceptions. Fifth, Method 1 is the only method that produces a large error when the angle of rotation becomes $>10^\circ$. This is because DIC inherently can only recover linear shifts and a large rotation cannot be fully recovered. Sixth, Method 3 performs the worst against the other two methods when the angle

of rotation is $<1^\circ$. This is because Method 3 relies on the accurate identification of the coordinates of the centroids of the particle and the associated circular colour adhesives, all of which are prone to error due to colour channelisation and binarisation. These errors hinder the ability of Method 3 in predicting small particle rotation ($<1^\circ$), particularly for low-resolution particles.

The error calculated in Figure 10 only accounts for errors associated with calculation of pure rotation and ignores the contribution of translation estimation errors. This is acceptable for Method 2 and Method 3 where the cropping process would remove any translation. However, the separation of the translation and rotation movements from the DIC displacement vectors could result in a larger error for Method 1. Figure 11 compares the error calculated by using Method 1 for pure rotation and rotation with translation. As expected, the comparison reveals that the error is slightly larger for rotation with translation than pure rotation.

Another potential error associated with Method 1 could arise from the selection of parameters for DIC analysis. The most important parameters are the initial interrogation window size and window deformation; these are critical if Method 1 is adopted to calculate large particle rotation ($>10^\circ$). The error of the calculated particle rotation by using Method 1 for pure rotation with different sets of parameters for DIC analysis is presented in Figure 12. Besides the variables, all DIC analyses are carried out with standard fast Fourier transform

correlation and adaptive evaluation method with a final interrogation window size of 32 px and 50% overlap. Three main points can be summarised from Figure 12. First, window deformation improves the accuracy of calculating particle rotation. Second, if possible, the initial interrogation window size should be close to or larger than four times the expected largest displacement between images and at the same time be sufficiently small to capture rotation since smaller initial interrogation window size could lead to underestimation of particle rotation (Chen *et al.*, 2016). Third, the percentage error for 10° rotation is significantly smaller than that for 20° rotation; this further demonstrates the limitations discussed above for DIC analysis.

Based on the error analysis results, it can be conservatively concluded that the developed methods have the ability of calculating particle rotation to the accuracy of $\pm 1^\circ$ for a minimum particle resolution of 30 px. This error should be satisfactory for most particle kinematics analysis in geotechnical applications.

5.2 Pros and cons of the three methods

The ultimate goal of the present research is to combine the techniques developed and apply them to investigate particle kinematics of natural sand for geotechnical applications. The pros and cons of each method discussed in this section are, therefore, assessed based on their applicability to analysis of ‘natural’ sand.

5.3 Accuracy

The majority of particle kinematics analyses for geotechnical applications do not require the accuracy of the measurement of particle rotation to be $<1^\circ$ (Andò *et al.*, 2012). In this case, all three methods can satisfy the accuracy requirement, provided the particle resolution is ≥ 30 px. Method 1 also requires that the maximum rotation between any two consecutive images be $<10^\circ$. For applications where it is important to capture particle rotation to the accuracy of 0.1° , Method 1 and Method 2 are preferable since Method 3 produces larger errors for small particle rotations. However, improving particle resolution always improves the prediction accuracy.

5.4 Resolution

The minimum required particle resolution for Method 1 is 30 px due to the minimum interrogation window size requirement for DIC analysis to capture rotation movement. For Method 2 and Method 3 it is feasible, though not recommended, to have lower particle resolution (<30 px) since the error becomes large for small particle rotation when particle resolution is set at 30 px (Figure 10(f)).

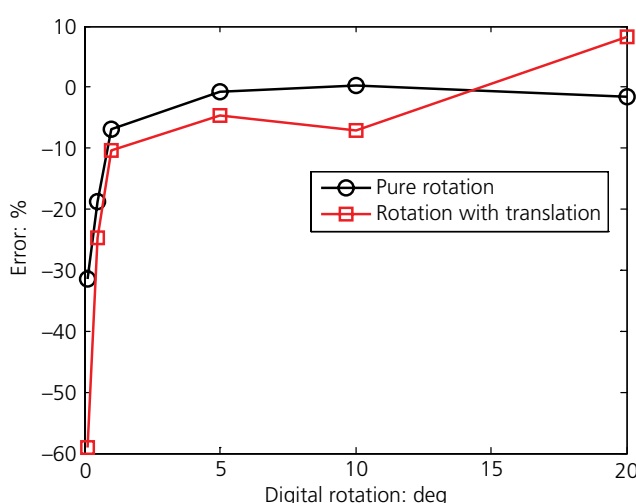


Figure 11. Percentage error of the calculated particle rotation of PDR 120 px using Method 1 against: (a) a set of digital rotation and (b) a set of digital rotation with translation (5 px vertical and 5 px horizontal) (positive indicates over-estimation and vice versa)

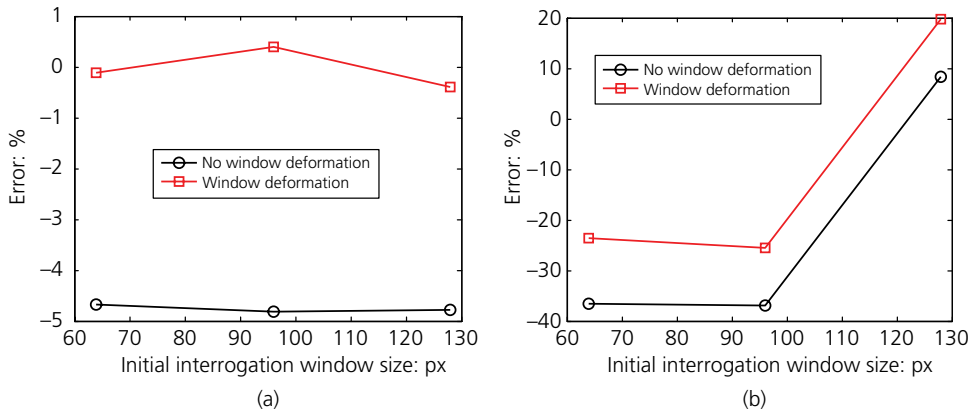


Figure 12. Percentage error of the calculated particle rotation of PDR 240 px using method 1 for pure rotation with different sets of parameters for DIC analysis: (a) 10° rotation and (b) 20° rotation (positive indicates over-estimation and vice versa)

Available commercial cameras have a maximum resolution from 25 to 200 Mpx. Considering that natural sand has a D_{50} of ~ 0.5 mm and assuming that a particle resolution is set at 30 px, an image of 28 000 to 220 000 sand particles can be obtained that is equivalent to a field view of 80×80 to 230×230 mm. Much larger fields of view will be possible in the not too distant future as camera technology advances rapidly.

5.5 Texture

Adequate texture or discernable features are required for the developed methods to calculate the particle rotation. Many natural sand particles naturally exhibit texture, and this facilitates the use of Method 1 and Method 2. Sand with poor texture can be enhanced for image analysis using spray paint. Method 3 requires two colour adhesives on the surface of each particle and given the size of natural sand this could not be manually accomplished; however, a micro-robotic printing process may be possible, though economically unfeasible, to achieve results with present technology. The technique may, however, be suitable for other scientific endeavours.

5.6 Memory requirements

The required computing memory for each method varies significantly. Assuming the obtained colour images have resolution of 25 Mpx, Method 3 requires the storage of the cropped colour images of each individual particle. Each calculation requires two colour images, and each 25 Mpx colour image requires a storage space of ~ 90 MB. Therefore, the computing memory needed for storing all the cropped colour

particle images using Method 3 is 180 MB. Method 2 requires the storage of the cropped grey-scale images of each individual particle. Each 25 Mpx grey-scale image requires a storage space of ~ 25 MB; thus, the computing memory for each calculation using Method 2 is reduced to 50 MB. Unlike Method 2 and Method 3, Method 1 does not require the storage of any cropped images of individual particles; instead it requires the storage of DIC analysis results for all image pairs. Each DIC analysis results for a pair of 25 Mpx images typically require a storage space of 1 MB. This means Method 1 requires significantly less computing memory than Method 2 and Method 3 for each calculation. The estimates of memory requirements for the three methods based on the number of particles are summarised in Table 2, assuming a particle resolution of 30 px.

5.7 Other factors

Each of the proposed methods has the potential to be applied to study particle kinematics of natural sand; however, one must select the most suitable method based on the specific application and available resources. In this study, the developed particle rotation algorithms were tested using spherical particles due to the difficulty in segmenting densely packed irregular-shaped particles. Nevertheless, the developed algorithms can be used to calculate particle rotation of irregular-shaped particles if particles can be identified correctly prior to particle tracking.

One limitation of Method 2 is that the image registration algorithm employed by the inbuilt Matlab function does not guarantee a global maximum, and this may lead to wrong

	Required camera resolution	Method 1	Method 2	Method 3
1 particle	Any	0·05 kB	1 kB	4 kB
25 000 particles	22·5 Mpx	1·25 MB	50 MB	200 MB
200 000 particles	180 Mpx	10 MB	400 MB	1·6 GB

Table 2. Memory requirements for three proposed methods

prediction of particle rotation if a local maximum is reached. In the authors' experience this does not happen often for particle images of unique textures; however, if it happens it is difficult to distinguish which particle image pair may have a local maximum rather than global maximum.

6. Selected results

Preliminary experimental results are presented in this section, where assemblies of dual-sized plastic circular rods were placed in a plane strain chamber to simulate both active and passive conditions (Table 1).

Particle trajectories of tracked particles from $\Delta/H=0$ to $\Delta/H=0\cdot05$ ($2\cdot87^\circ$) for all four tests are shown in Figure 13. The solid dots in Figure 13 represent the starting positions of the particle centroids identified in the initial images. A concentration of displacement in a wedge-shaped region beside the wall is clearly observed in all the four tests. Beyond these wedges, very little displacements are observed. For active tests (Figure 13(a) and 13(b)), particles within the active wedge follow closely to the movement of the wall, where particles close to the wall move primarily in an outward horizontal direction, and particles further out move downwards at an angle inclined to the wall. For passive tests (Figure 13(c) and 13(d)), particles within the passive wedge move upwards at an inclined angle and follow closely to the movement of the wall. The upward particle movement at the top layer suggests that the lateral force overcame the applied surcharge; however, this does not affect the efficacy of the developed analytical approaches. No significant differences in particle trajectories are observed between smooth and rough wall tests.

The displacement fields obtained from DIC analysis from all four tests are used to calculate the maximum natural shear strains (Figure 14) and element rotations (Figure 15) using finite strain theory (Omidvar *et al.*, 2014). Note that the calculated strain and rotation maps are based on the displacement vectors obtained from DIC analysis between the initial and final image of each test, even though many more strain increments exist. In addition, due to the large size of the employed HDPE rods, the meshes used in this study to generate shear

strain and element rotation maps are much coarser than other similar studies using natural sand or other granular materials such as glass beads. As a result, the obtained shear strain maps (Figure 14) and element rotation maps (Figure 15) may appear coarser than similar results reported in literature. For a smooth wall under active condition, Figure 14(a) shows a concentration of intense shear within a linear sliding wedge from the toe of the wall to the surface that is approximately inclined at 56° to the horizontal. This observation agrees well with Rankine's theory of active earth pressure where $\theta=45+\phi/2$, and $\phi=16^\circ$ is the friction angle of the testing material. For a smooth wall under passive condition, Figure 14(c) also shows a concentration of intense shear within a linear wedge that is approximately inclined at 41° to the horizontal though the wedge starts at about $2/5$ of the wall height and could be a result of insufficient confining pressure. Compared with smooth wall tests, the shear maps of rough wall tests for both active (Figure 14(b)) and passive conditions (Figure 14(d)) display a wider shear region and a more blurred sliding wedge. However, the calculated shear strains adjacent to the wall show very little difference between the smooth and rough wall tests. The element rotation maps (Figure 15) for all four tests mimics the patterns of the shear strain maps where large rigid body rotation occur in regions of significant shear strains with a maximum rotation of $\sim 15^\circ$.

Particle rotation in degrees from $\Delta/H=0$ to $\Delta/H=0\cdot05$ ($2\cdot87^\circ$) for all four tests are shown in Figure 16. A number of interesting observations can be made. First, large particle rotation occurs in regions roughly corresponding to those where shear strain localises. Second, the magnitude of the calculated particle rotation is significantly higher than the calculated rigid body rotation. This is expected because the element rotation is calculated based on a triangle element that represents an area of at least a few particles; hence, the calculated rigid body rotation is the average rotation of the area. Third, particles adjacent to the rough walls for both active and passive conditions show larger particle rotations than those in smooth wall tests, indicating that the rough interface promotes more particle rotation and/or rolling than sliding. Fourth, for active tests, the outwards movement of the wall promotes primarily clockwise rotations for particles adjacent to the wall, while for

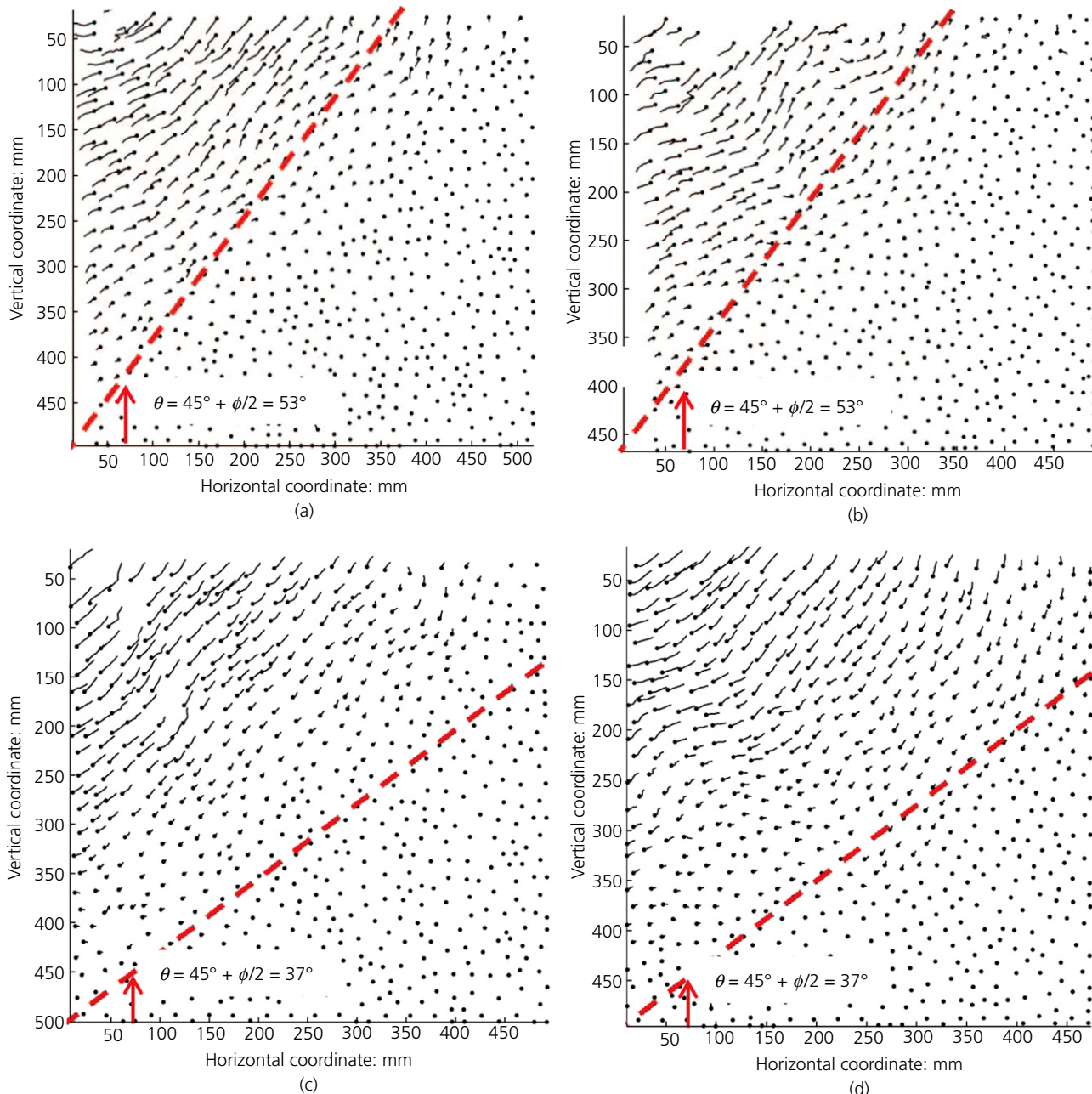


Figure 13. Particle trajectories for $\Delta/H = 0.05$ (2.87°): (a) test 1 (active, smooth wall), (b) test 3 (active, rough wall), (c) test 2 (passive, smooth wall) and (d) test 4 (passive, rough wall)

passive tests the inwards movement of the wall promotes primarily counter-clockwise rotations. Fifth, multiple particle rotation pairs can be found in Figure 16 where a particle rotation in clockwise direction is accompanied by adjacent counter-clockwise particle rotation.

7. Conclusions

This paper presents three new methods to quantify particle rotations under plane strain conditions. Based on the experiments conducted in this study, the developed methods

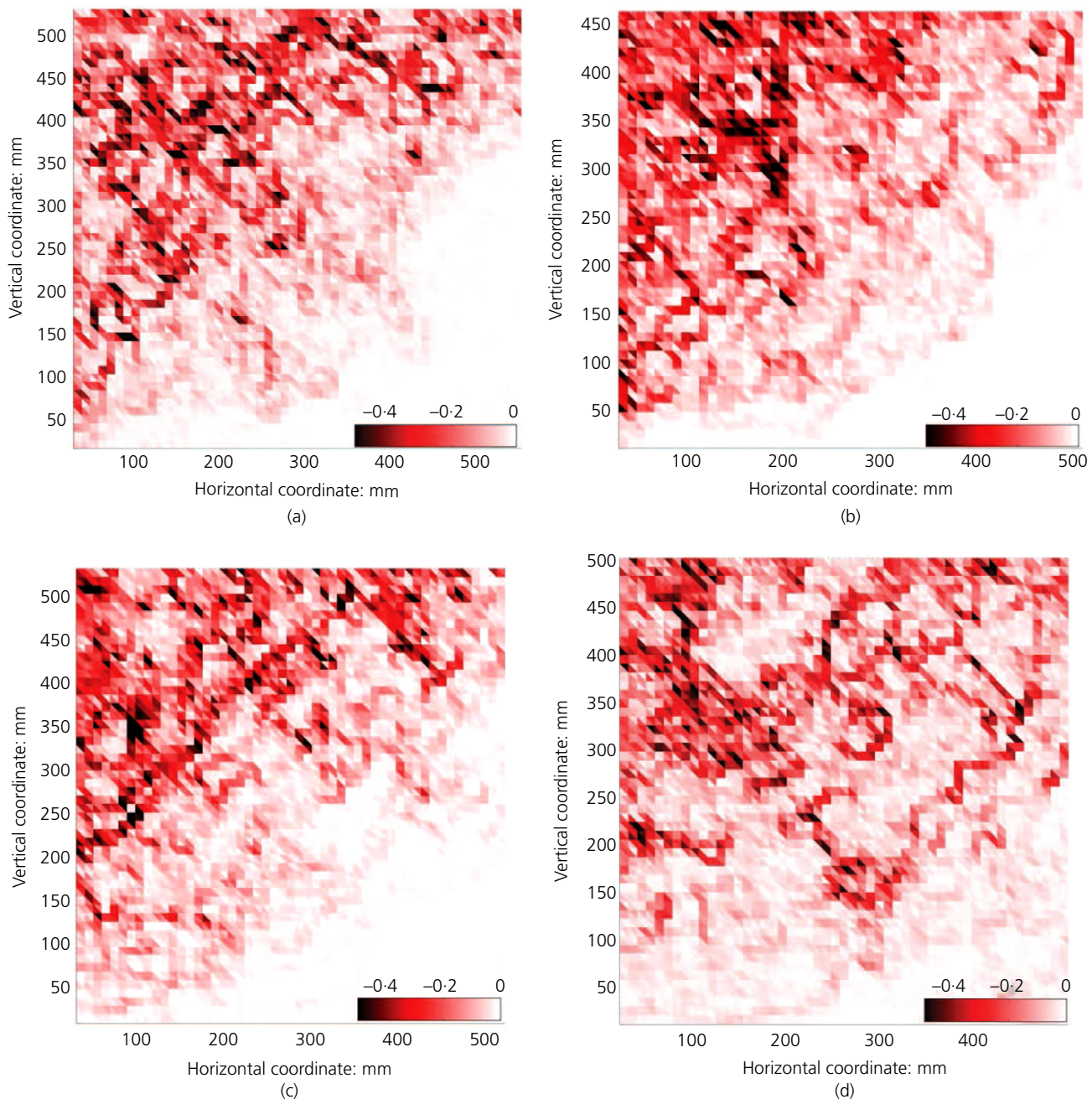


Figure 14. Shear strain map for $\Delta/H = 0.05$ (2.87°): (a) test 1 (active, smooth wall), (b) test 3 (active, rough wall), (c) test 2 (passive, smooth wall) and (d) test 4 (passive, rough wall)

calculate particle rotations to a minimum accuracy of $\pm 1^\circ$, provided the particle resolution is ≥ 30 px. Higher accuracy can be achieved with greater particle resolution. The developed methods combined with particle identification and tracking have been applied successfully to study particle kinematics of

granular assemblies in a plane strain chamber against a wall subjected to wall rotation about its toe. Significant particle rotations are observed in the regions of intense shear. Particles adjacent to a rough wall also have shown larger rotations than particles adjacent to a smooth wall; this indicates wall

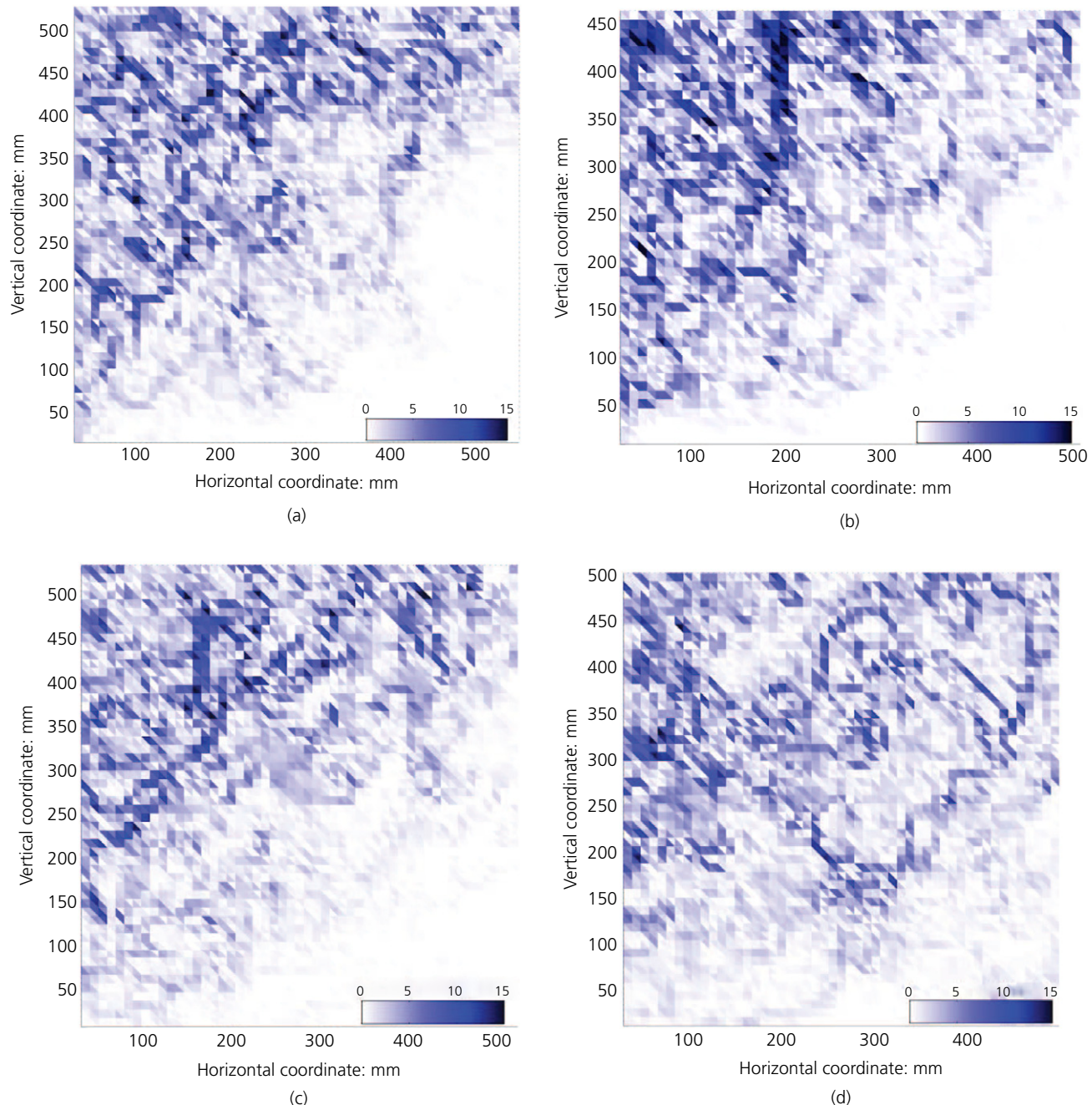


Figure 15. Rigid body rotation map in degrees for $\Delta/H = 0.05$ (2.87°): (a) test 1 (active, smooth wall), (b) test 3 (active, rough wall), (c) test 2 (passive, smooth wall) and (d) test 4 (passive, rough wall)

roughness promotes particle rotation and/or rolling relative to sliding. These interesting particle-level observations highlight the importance of particle kinematic analysis to achieve a deeper understanding of the behaviour of granular materials.

All developed algorithms are included in the open-source software ‘MAGICgeo’ (Multi-scale Analysis for Granular Image Correlation) developed at New York University and this can be found in NYU (2016).

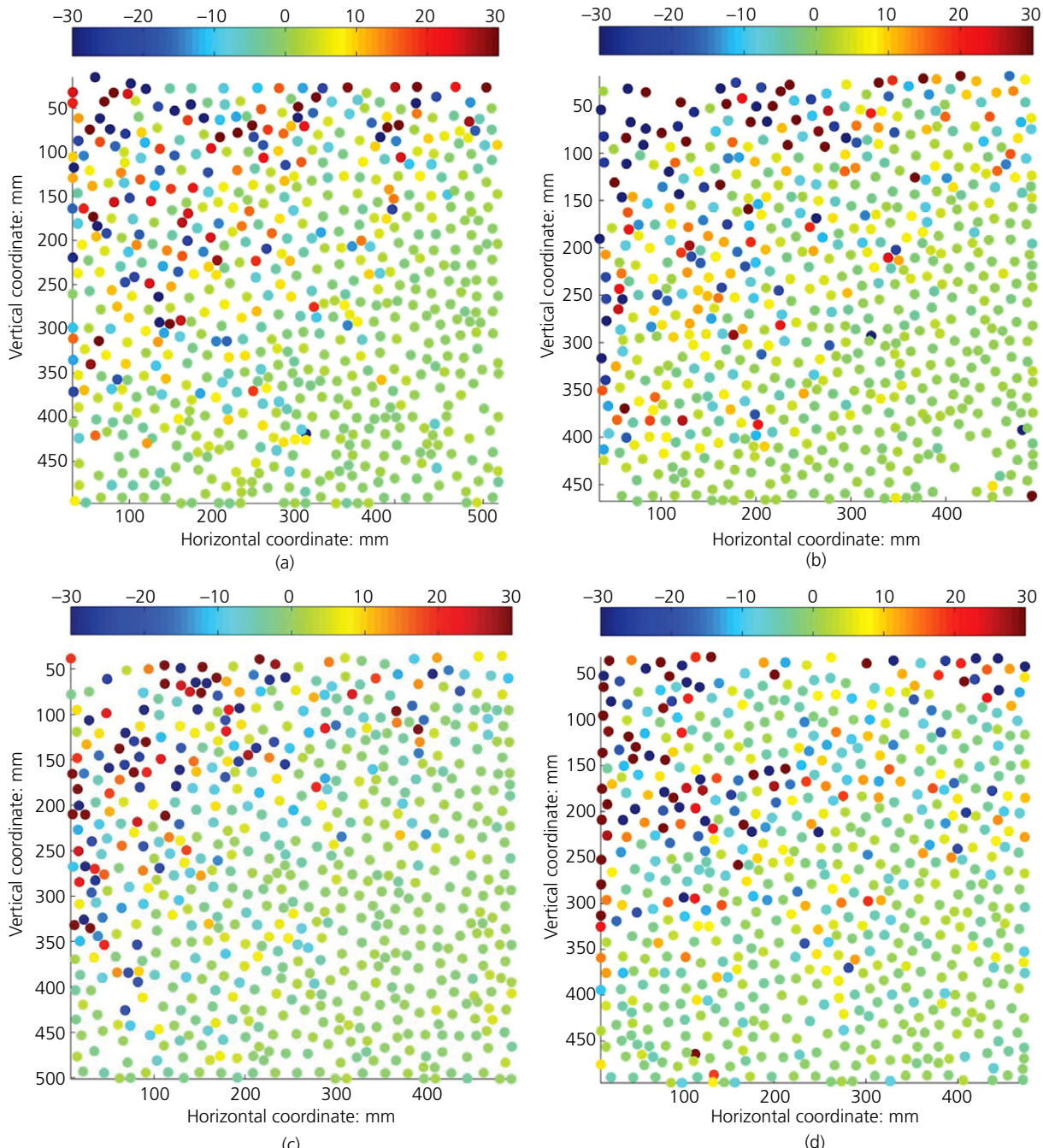


Figure 16. Particle rotation in degrees for $\Delta H = 0.05$ (2.87°):
(a) test 1 (active, smooth wall), (b) test 3 (active, rough wall),
(c) test 2 (passive, smooth wall) and (d) test 4 (passive, rough

wall) (positive indicates counter-clockwise and negative indicates clockwise)

Acknowledgements

The authors gratefully acknowledge the support of the Defense Threat Reduction Agency (DTRA) of the USA, grant number

HDTRA1-10-1-0049. This work was also partially supported by NSF grant DRL1417769, and the Materials Research Science and Engineering Center (MRSEC) program of the National Science Foundation under Award Number

DMR-1420073. The authors are also thankful to Dr Stephan Bless for his valuable comments.

REFERENCES

- Andò E, Hall SA, Viggiani G, Desrues J and Bésuelle P (2012) Grain-scale experimental investigation of localised deformation in sand: a discrete particle tracking approach. *Acta Geotechnica* **7**(1): 1–13.
- Atherton TJ and Kerbyson DJ (1999) Size invariant circle detection. *Image and Vision Computing* **17**(11): 795–803.
- Bardet JP and Proubet J (1992) Shear-band analysis in idealized granular material. *Journal of Engineering Mechanics* **118**(2): 397–415.
- Baudet B, Bolton M and Clayton C (2010) Soil mechanics at the grain scale: issue 1. *Geotechnique* **60**(5): 313–314, <http://dx.doi.org/10.1680/geot.2010.60.5.313>.
- Carpenter AE, Jones TR, Lamprecht MR et al. (2006) CellProfiler: image analysis software for identifying and quantifying cell phenotypes. *Genome Biology* **7**(10): R100.
- Chen Z, Li K, Omidvar M and Iskander M (2016) Guidelines for DIC in geotechnical engineering research. *International Journal of Physical Modelling in Geotechnics*, <http://dx.doi.org/10.1680/jphmg.15.00040>.
- Crocker JC and Grier DG (1996) Methods of digital video microscopy for colloidal studies. *Journal of Colloid and Interface Science* **179**(1): 298–310.
- Hall SA, Bornert M, Desrues J et al. (2010) Discrete and continuum analysis of localised deformation in sand using X-ray µCT and volumetric digital image correlation. *Geotechnique* **60**(5): 315–322, <http://dx.doi.org/10.1680/geot.2010.60.5.315>.
- Hunter GL, Edmond KV, Elsesser MT and Weeks ER (2011) Tracking rotational diffusion of colloidal clusters. *Optics Express* **19**(18): 17189–17202.
- Mathworks (2006) <http://www.mathworks.com/help/images/ref/regionprops.html> (accessed 17/10/2016).
- Mathworks (2013) <http://www.mathworks.com/help/images/ref/imregtform.html> (accessed 17/10/2016).
- Matsuoka H (1974) A microscopic study on shear mechanism of granular materials. *Japanese Society of Soil Mechanics and Foundation Engineering* **14**(1): 29–43.
- NYU (2016) <http://wp.nyu.edu/magicgeo> (accessed 17/10/2016).
- Oda M and Kazama H (1998) Microstructure of shear bands and its relation to the mechanisms of dilatancy and failure of dense granular soils. *Geotechnique* **48**(4): 465–481, <http://dx.doi.org/10.1680/geot.1998.48.4.465>.
- Oda M and Konishi J (1974) Microscopic deformation mechanism of granular material in simple shear. *Japanese Society of Soil Mechanics and Foundation Engineering* **14**(4): 25–38.
- Oda M, Konishi J and Nemat-Nasser S (1982) Experimental micromechanical evaluation of strength of granular materials: effects of particle rolling. *Mechanics of Materials* **1**(4): 269–283.
- Omidvar M, Iskander M and Bless S (2012) Stress-strain behavior of sand at high strain rates. *International Journal of Impact Engineering* **49**: 192–213.
- Omidvar M, Chen Z and Iskander M (2014) Image-based Lagrangian analysis of granular kinematics. *Journal of Computing in Civil Engineering* **29**(6): 04014101.
- Paikowsky SG and Xi F (2000) Particle motion tracking utilizing a high-resolution digital CCD camera. *Geotechnical Testing Journal* **23**(1): 123–134.
- Peng T, Balijepalli A, Gupta SK and LeBrun T (2007) Algorithms for on-line monitoring of micro spheres in an optical tweezers-based assembly cell. *Journal of Computing and Information Science in Engineering* **7**(4): 330–338.
- Rasband WS (1997–2016) ImageJ. U.S.National Institutes of Health, Bethesda, MD, USA. See <http://imagej.nih.gov/ij/> (accessed 17/10/2016).
- Rechenmacher A, Abedi S and Chupin O (2010) Evolution of force chains in shear bands in sands. *Geotechnique* **60**(5): 343–351, <http://dx.doi.org/10.1680/geot.2010.60.5.343>.
- Roscoe KH and Schofield AN (1964) Discussion of Rowe 1963. *Journal of the Soil Mechanics and Foundations Division, ASCE* **90**(1): 136–150.
- Terzaghi KV (1920) Old earth pressure theories and new test results. *Engineering News Record* **85**(14): 632–637.
- Umeyama S (1991) Least-squares estimation of transformation parameters between two point patterns. *IEEE Transactions on Pattern Analysis and Machine Intelligence* **13**(4): 376–380.
- von Pokorný ML and Horender S (2014) Measurement of particle rotation in a saltation layer. *Earth Surface Processes and Landforms* **39**(13): 1803–1811.
- Yuen HK, Princen J, Illingworth J and Kittler J (1990) Comparative study of Hough transform methods for circle finding. *Image and Vision Computing* **8**(1): 71–77.
- Zheng J and Hryciw RD (2016) Segmentation of contacting soil particles in images by modified watershed analysis. *Computers and Geotechnics* **73**: 142–152.

HOW CAN YOU CONTRIBUTE?

To discuss this paper, please email up to 500 words to the editor at journals@ice.org.uk. Your contribution will be forwarded to the author(s) for a reply and, if considered appropriate by the editorial board, it will be published as discussion in a future issue of the journal.

International Journal of Physical Modelling in Geotechnics relies entirely on contributions from the civil engineering profession (and allied disciplines). Information about how to submit your paper online is available at www.icevirtuallibrary.com/page/authors, where you will also find detailed author guidelines.